Microstructure evolution and tensile behaviour of fine-grained 6082 Al wire with high ultimate strength and high work hardening by friction stir extrusion of bulk Al sheet

Liang Yuan[1, 3], Xun Zeng[1], Xingjian Zhao[1], Yanheng Xie[1], Joao Gandra[2], Dikai Guan[1,4*]

[1]Department of Materials Science and Engineering, University of Sheffield, Sheffield S1 3JD, UK

[2]TWI, Granta Park, Great Abington, Cambridge, CB21 6AL, UK

[3]College of Bioresources Chemical and Materials Engineering, Shaanxi University of Science and Technology, Xi'an, 710021, China

4 Department of Mechanical Engineering, School of Engineering, University of Southampton, Southampton SO17 1BJ, UK

*Corresponding author, E-mail address: dikai.guan@soton.ac.uk

Abstract: Driven by the highly enhanced demand for metallic materials with excellent strength-ductility synergy, fine-grained alloy fabricated by severe plastic deformation (SPD) is a long-lasting research interest**.** In this study, a fine-grained aluminium (Al) alloy wire with high ultimate tensile strength (316.8 MPa) and high work hardening capability (n=0.34) was developed via a novel bulk-consolidation friction stir extrusion (FSE) enabled by CoreFlow^{TM} process based on FSE processed 6082-T6 Al sheet. Grain refinement of 200 times occurred in CoreFlowed Al alloy, which is rarely observed in FSEed Al alloy counterpart based on milling metal chips. The undesirable feature of coarse and preferred secondary phase particles in the initial 6082-T6 Al billet was well tailored during CoreFlow^{TM} process, which led to an attractive characteristic of dispersed and refined particle phases in CoreFlowed Al alloy. Texture components of S (V=8.24%) and Goss

(V=6.86%) were observed, however, the overall micro-texture intensity of CoreFlowed Al wire was significantly weakened. Due to the cooperative deformation modes consisting of dislocation slip and grain boundary sliding, as well as the positive compatibility effect of fine-grains on deformation, CoreFlowed Al specimens demonstrated an excellent ductility (EI=19.3%) and acceptable yield strength (YS=182 MPa) compared to initial 6082-T6 Al sheet (EL=10.4%, and YS=225 MPa). Benefiting from the higher work hardening capability, the final ultimate tensile strength (UTS) of CoreFlowed Al (316.8 MPa) reached almost the same level as the 6082-T6 Al sheet (324.6 MPa). Furthermore, after one simple post-processing one-step heat treatment (175 ^{o}C for 10 h), the wire's yield strength was improved to 250 MPa, although only maintaining 9% elongation. This low elongation could be attributed to micro-cracks induced by coarsening of the second phases, while high yield strength resulted from fine grain size and precipitate strengthening. The wide range of variations in the mechanical properties of CoreFlowed Al wire under different conditions provides significant freedom in tailoring the mechanical properties of alloy wire in applications.

Keywords: CoreFlow^{TM}, 6082 Al alloy wire, Grain refinement, Secondary phase particles, Ductility, Work hardening capability

1. Introduction

Severe plastic deformation (SPD) techniques among various deformation processes have been intensively applied to metals and alloys to achieve a refined microstructure, thereby enhancing the mechanical properties of alloy materials [1-8]. Although the most common applications of Al alloys are as cast or wrought articles, Al alloy wires fabricated via different SPD methods have also received considerable attention in the field of wire-based additive manufacturing (AM) [9] and the welding industry [10], owing to their high strength-to-weight ratio, good corrosion resistance, good weldability and low cost. In the past decades, sustained effort has been devoted to improving the processing route of alloy wires. Until now, several methods, such as hot extrusion [11], drawing [12, 13], friction stir extrusion (FSE) [14] and derivative of FSE [15, 16], have been utilized to produce alloy wires or tubes from recycled milling metal chips, powder and billet.

Using low-cost precursors of powders or the recycled metal wastes of machining chips as raw materials, the novel FSE process among these above-mentioned methods seems to be a promising technique in the fabrication of alloy wires due to its low cost and high quality [17]. The FSE has recently been utilized successfully to extrude multiple metal wires, such as Al-based alloys (AA2xxx, AA6xxx, and AA7022) [18-20], pure Mg [21], Mg-based alloy [22] and SiCp/Al composite [23]. This process has been applied to several metallic materials leading to significant grain refinement and enhancement in mechanical properties. For example, the grain of FSE processed Al wire (16 μm) was less than

one-tenth of that of the initial material (179 μm) [24]. Grain refinement of about 10 times was obtained in FSEed Mg-RE alloy wire, which resulted in the increased yield strength and compression strain by 42.5% and 35.5%, respectively [25]. Another striking feature of FSEed alloy wires is weak texture [24, 26], even though the material suffers heavy deformation containing rotational shear and linear extrusion during FSE. However, the wires produced by the FSE process normally show a very short length due to a small-sized container where metal chips are pre-filled, restricting a wide range of applications of FSE process.

CoreFlow™ was invented by the Welding Institute (TWI) to produce closed sub-surface channels in components for internal cooling systems, heat exchangers and integrated fluid management. The wires extruded by CoreFlow™ processing are the byproduct of this process. Nevertheless, CoreFlow™ has been proven to be an innovative bulk-consolidation FSE technique to produce bespoke wires. CoreFlow™ is capable of extruding wires with unlimited length at room temperature from a plate in a single step as long as the supplied bulk alloy plate is large enough, thereby having the potential to significantly reduce the product cost and save energy compared to traditional wire drawing or extrusion techniques, and overcome the challenge of the limited length of wires produced by other FSE techniques. It is believed that there are considerable differences between bulk alloy sheets and milling/machining alloy chips, such as internal stress, specific surface area and microstructure. The question therefore arises: how does the microstructure of novel CoreFlowed alloy evolve when a rotating die was plunged into an alloy sheet rather than chips or powders? Does the severe plastic deformation

affect recrystallization behaviour during the extraction of bulk material by spiral grooves towards the hollow centre of the die? As an emerging of the novel process, however, these issues on CoreFlowed alloy have not been systematically investigated.

Since CoreFlow^{TM} process is a novel SPD technology which combines both thermal and mechanical effects via a rotating tool, this process may be an effective method to optimize the mechanical properties through manipulating the microstructural parameters such as the grain size, the density and types of precipitates and the distribution of second phases by breaking up grains and particles in comparison with other SPD methods. It has been reported [27] that the fine equiaxed grains and the dispersed precipitates (W-phase, I-phase and LPSO) were helpful to improve the tensile properties of FSPed Mg-Zn-Y-Zr alloy through the friction stir process. As we know, 6xxx Al (Al-Mg-Si) alloy with medium-strength is a heat-treatable Al alloy, especially, AA6082 alloy, which is the strongest in the 6000 family [28, 29]. The strength of 6xxx Al alloys is achieved by ageing after solution heat treatment followed by a rapid water quench [30]. The precipitation sequence in 6xxx Al alloys is universally considered as α → solute clusters → GP zones → β′′ → β′ → β [31]. Owing to the friction stirring heat, the strengthening metastable β′′ phase (Mg_5Si_6) had transformed into coarse stable β-Mg_2Si phase [32]. Meanwhile, the Fe- and Cr-rich coarse grain-boundary particle phases still retain in alloy matrix at the high temperature of 416 ^{o}C [32]. These coarse particle phases may become the nucleation site of small cracks [33]. Therefore, to understand the overall mechanical behaviour of CoreFlowed Al alloys containing particle phases, a detailed understanding of the evolution behaviour of secondary phase particles is necessary. However, little is

understood regarding the evolution of secondary phase particles during processing of CoreFlow™.

It is widely reported that the strength or hardness of conventional polycrystalline metals increases with decreasing grain sizes, known as the classical Hall-Petch relationship [33]. However, the softening phenomenon occurring in some fine-grained zones was also reported by Liang et al. [34] and Naumov et al. [35] due to the dissolution or growth of the strengthening phases, although the grain size of alloy material in nugget zone after FSW was refined significantly. In other words, the Hall-Petch strengthening in those fine-grained microstructures is not a dominant strengthening mechanism compared to the precipitation strengthening mechanism. Moreover, the small and equiaxed grains in the stir zone (SZ) obtained after friction stir processing (FSP) of SPD technology display some different deformation modes from the dominated basal slip into the dominated {10-12} twinning along the processing direction in the SZ, which was attributed to the inhomogeneous of microstructure, texture and dislocation density in these different fine-grained regions [36]. Since the slip-induced grain boundary sliding (GBS) was considered to accommodate the incompatibility of plastic strain at grain boundaries [37], it is reasonable to speculate that the GBS may be activated in the presence of anisotropic dislocation slip to accommodate plastic deformation, leading to an abnormal Hall-Petch relationship. The microstructure formed via a novel CoreFlow™ technology which combines both thermal and mechanical effects may be accompanied by different deformation characteristics during elevated strain. Hence, investigating the mechanical response to illustrate deformation mechanism, and thus improving the

mechanical properties of CoreFlowed alloy is recognized as being of great importance.

In the present work, the 6082 Al alloy wire fabricated via CoreFlow™ was selected to investigate the microstructure evolution and its mechanical response. The evolution of grain and micro-texture, variation of particle phases, tensile properties at room temperature, and corresponding deformation mechanism were addressed in detail. One-step ageing treatment was performed on the post-CoreFlowed Al alloy wire to adjust mechanical properties. The underlying mechanisms responsible for the change in mechanical properties were analysed.

2. Materials and methods

The material for fabricating the alloy wire samples used in this study was an AA 6082 sheet with dimensions of 300 x 300 x 10 mm^3, whose chemical composition is listed in Table 1. The T6 treatment is applied to the raw 6082 Al alloy sheet before the CoreFlow™ processing. The CoreFlowed 6082 Al wires having 2 mm diameter and 400 mm length used in this work were provided by TWI Inc., UK. The schematic diagram of the CoreFlow™ process was shown in Fig. 1a. A stationary shoulder is employed to confine the nugget of viscoplastic material, limiting the flow of material extracted by the probe. With the appropriate rotation direction, the geometrical features of the probe cause part of the nugget material to be conveyed into the shoulder. As the tool assembly traverses along a pre-defined path, the process of extracting the material leads to the formation of i) extruded alloy wire, i.e. CoreFlowed wire (top in Fig. 1a), and ii) a closed sub-surface channel within the workpiece (bottom in Fig. 1a).

Table 1 Composition of the 6082 Al alloy (in wt.%)

Element	Mg	Si	Mn	Fe	Cr	Cu	Zn	Al
Content	0.93	0.89	0.58	0.30	0.06	0.04	0.04	Bal.

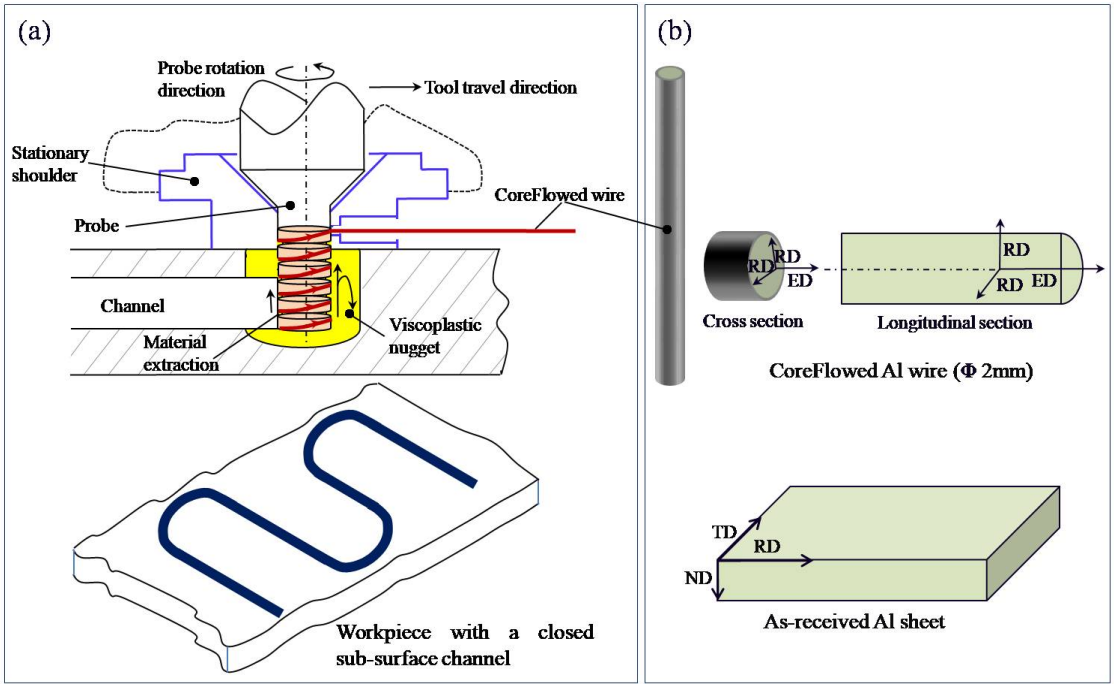

Fig. 1 Schematic illustrations of the CoreFlow™ process based on alloy sheet (a) and EBSD test surface marked by light green on Al sheet and CoreFlowed Al wire (b).

The micro-hardness (H_V) of the alloy samples with different states was determined by Vickers hardness tester (model Mitutoyo) at room temperature, and the H_V average value was calculated from ten indentations under a load of 500 g and a dwell time of 15 s. The mechanical properties of the Al alloy samples were measured by uniaxial tensile tests using dumbbell-shaped specimens with a gauge length of 12 mm and a gauge diameter of 1.2 mm. The dumbbell-shaped tensile samples were cut by electrical discharge machining (EDM) from the different Al alloys including as-received 6082 Al sheet along RD, as-received CoreFlowed Al wire and aged Al wire. The tensile tests were carried out on a Deben CT500N in situ tensile machine with a testing speed of 1.0×10^{-3} s^{-1} at ambient temperature. Before testing, the tensile samples were polished by using P2500 grit SiC

grinding paper to remove the possible oxidation layer at the surface, and tensile tests were performed for at least three times in order to ensure its precision.

Phase identification in alloy samples was carried out by X-ray diffraction (XRD) on PANalytical Aeris with Cu-*K*α radiation source at 40 kV and 30 mA, and in the range of 10-100^{o}. The microstructure analyses were carried out by a FEI Inspect F7900 field emission gun scanning electron microscope (FEG-SEM) fitted with an Oxford Instrument electron back scatter diffraction detector operating at 20 kV with a step size of 1 µm. The EBSD samples were cut from as-received CoreFlowed Al wires along perpendicular to (cross section) and parallel to (longitudinal section) the extrusion direction of CoreFlowed Al wire, respectively, as shown in Fig. 1b. The EBSD samples were carefully mechanically ground and polished using P1200, P2500, P4000 SiC paper, 1 µm, 0.25 µm oil-based diamond suspension, 40 nm OPS suspension, and followed by ion polishing with a Gatan PECS II ion polishing system under a condition of 5 kV, 4^{o} for 30 min. The analysis of EBSD data was carried out using HKL-Channel 5 post-processing software. To eliminate spurious boundaries caused by orientation noise, the boundary misorientation of less than 2° was cutoff. Grain boundaries with misorientation larger than 15° were defined as high-angle grain boundaries (HAGBs) and those of misorientation between 2° and 15° as low-angle grain boundaries (LAGBs). Furthermore, to obtain a deeper insight into the nature of deformation in grains, the Kernel average misorientation (KAM) image and the corresponding Schmid factor (SF) image were also measured. To obtain a reliable GOS value, herein, the EBSD indexed area of as-received CoreFlowed Al sample is about 92% during the EBSD test.

3. Results and discussion

3.1. Hardness results

Compared to the micro-hardness (~113 HV) of the raw 6082-T6 Al sheet, the micro-hardness of the as-received CoreFlowed 6082 Al wire was ~53.36 HV (Fig. 2). It may be attributed to the dissolution of the partial precipitated hardening phases during CoreFlow™ processing. To strengthen the as-received CoreFlowed Al wire, precipitates were induced again by applying two different ageing treatments. As shown in Fig. 2, after a simple one-step ageing treatment without solution quenching, the micro-hardness of aged CoreFlowed Al wire jumps to the maximum value of ~105.25 HV, although slightly lower than that of the as-received 6082-T6 Al sheet. Based on the above analysis, the simple one-step ageing treatment at 175 °C for 10 h is selected to compare with the as-received CoreFlowed Al wire.

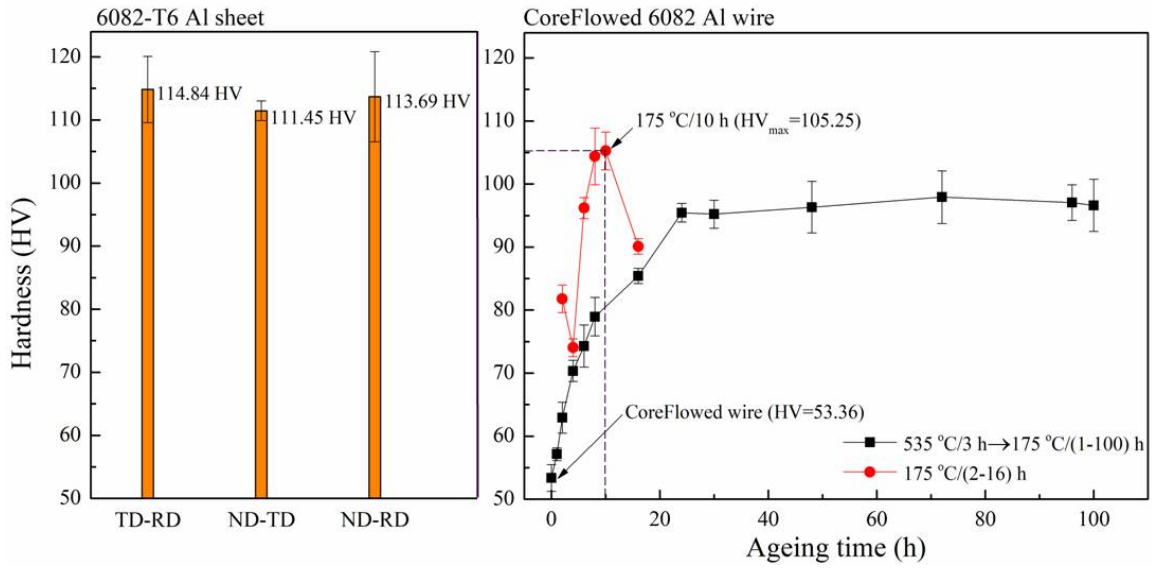

Fig. 2 Micro-hardness as a function of ageing time for as-received CoreFlowed Al wire, and the corresponding hardness of the initial 6082-T6 Al sheet along different planes.

3.2. Phase constitution

Fig. 3 shows the XRD peaks of the 6082 Al alloy subjected to different conditions. In addition to the primary γ-Al phase, the peak of Mg_2Si, AlMnSi and AlMn phase was also observed in as-received 6082-T6 Al alloy. It is reasonable to conclude that the precipitate strengthening is mainly responsible for the high strength of 6082-T6 Al alloy sheet, which was also confirmed by subsequent tensile stress-strain curve in Fig. 10a. After CoreFlow™ process, it is found that the diffraction peak intensity of three kinds of precipitates aforementioned, especially Mg_2Si and AlMn phase, decrease significantly in as-received CoreFlowed Al wire. Kalinenko et al. [32] predicted that the β-Mg_2Si phase was gradually dissolved above 300 ^{o}C, and it was expected to complete at 502.5 ^{o}C. During the CoreFlow™ process, the CoreFlowed Al sample experienced a temperature gradient range of 25-550 ^{o}C based on the result in [38]. Therefore, the partial dissolution of the β-Mg_2Si phase can occur. Moreover, it can reasonably speculated that the decrease in the volume fraction of AlMn phase during CoreFlow™ process may also be attributed to its dissolution based on result reported by Kumar et al. [39], although the accurate melting point of the AlMn phase is not yet known. The phase constitution and its intensity in aged CoreFlowed Al specimen after ageing at 175 ^{o}C for 10 h hardly changed compared to the as-received CoreFlowed Al specimen. It seems that the ageing treatment did not promote the formation of new precipitate phase. However, the occurrence of new phase, such as γ → G.P zone → β′′→ β′→ β, cannot be arbitrarily eliminated, since the solid phases in Al alloy, whether it is ageing precipitate (Mg_2Si phase) or secondary phase (AlMnSi and AlMn phase), are often in nanoscale, which is difficult to be detected via XRD analysis. For example, the average thickness of β′′ phase is only 3 nm in friction stir welding joint of

6082-T6 Al alloy [37].

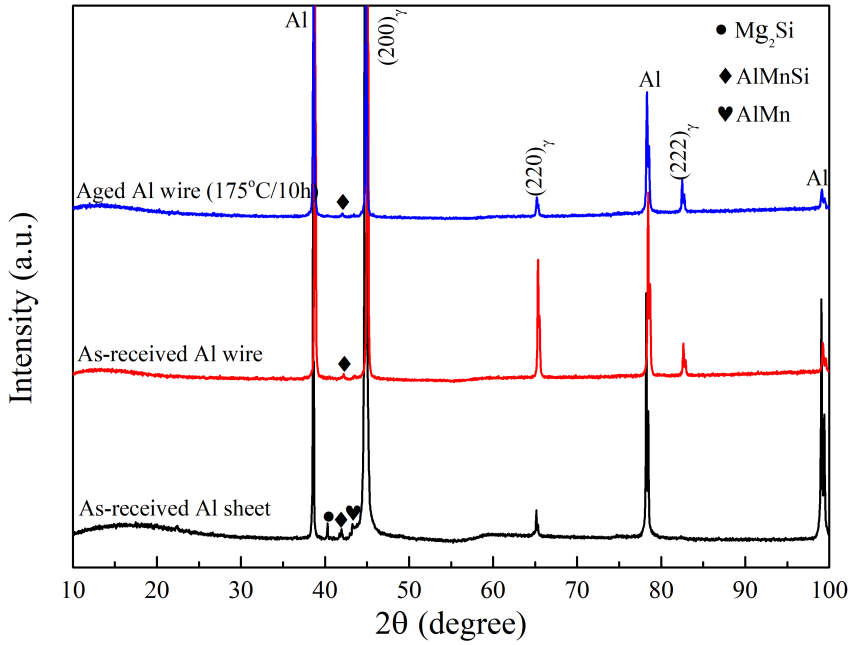

Fig. 3 X-ray diffraction patterns of Al alloy with different states.

3.3. Microstructure of CoreFlowed 6082 Al wire

3.3.1. Grain morphology

The EBSD inverse pole figure (IPF) maps of the as-received 6082-T6 Al sheet and CoreFlowed Al wire are shown in Fig. 4 and Fig. 5, respectively. The microstructure of the initial 6082-T6 Al alloy sheet along the ND-TD plane exhibits a bimodal-like characteristic. The bimodal-like microstructure comprising of large equiaxed grains of ~ 500 µm surrounded by fine equiaxed grains of ~ 30 µm is presented in Fig. 4a. In contrast, the extremely elongated grains appeared in the ND-RD (Fig. 4b) and TD-RD planes (Fig. 4c), respectively. These grains were heavily elongated up to about 2000 µm, which is similar to a typical rolled microstructure.

After processing of CoreFlow™ technology, however, the grain morphology of the extruded CoreFlowed Al wires was considerably different from that of the parent 6082-T6

Al alloy sheet. As seen from Figs. 5a and b, the grains were equiaxed with uniform sizes (~ 11.4 μm along cross-section and ~ 7.6 μm along longitudinal section). The grain refinement effect of the CoreFlow™ process is attributed to dynamic recrystallization (DRX) through the severe friction-shear effect and high friction heat input. Owing to the high stacking fault energy of Al with a FCC structure, a large number of dislocations climb and cross-slip can be easily activated, and thus dynamic recovery (DRV) and DRX become the dominant restoration mechanisms during the successive CoreFlow™ process. On the other hand, the uniformly-distributed second phase particles can also accelerate recrystallization via a particle-simulated nucleation mechanism. The redistribution of second-phase particles in the CoreFlowed Al specimen will be discussed in a later section. Moreover, the distribution of grain orientation along the longitudinal section is relatively more uniform than along the cross section due to the uniformly-distributed second phase particles, just as Shahsa et al. [27] found that the occurrence of particle phase-stimulated nucleation has an effect on randomizing the recrystallized grain orientation.

Comparatively, the magnitude of CoreFlow™ process on grain refinement is up to approximately 200 times in this work. Similarly, a significant grain refinement ranging from ~ 10 to ~ 50 times also occurred in the microstructure of the starting material after processing of FSE based on milling metal chips, but the extent of refinement is much lower compared to the CoreFlow™ process [16, 40, 41]. In the current work, the novel CoreFlow™ derived from FSE simply replaces the milling alloy chips with bulk alloy sheets, but actually the material flow resistance experienced in bulk Al sheet is slightly lower due to the lower hardness of the bulk sheet than those of the chips [42], which led to a

slightly lower temperatures experimentally from the CoreFlowed billet. As a result, the grain size in the bulk sample is smaller than that of the chips, although the initial grain size of the Al alloy sheet was considerably larger.

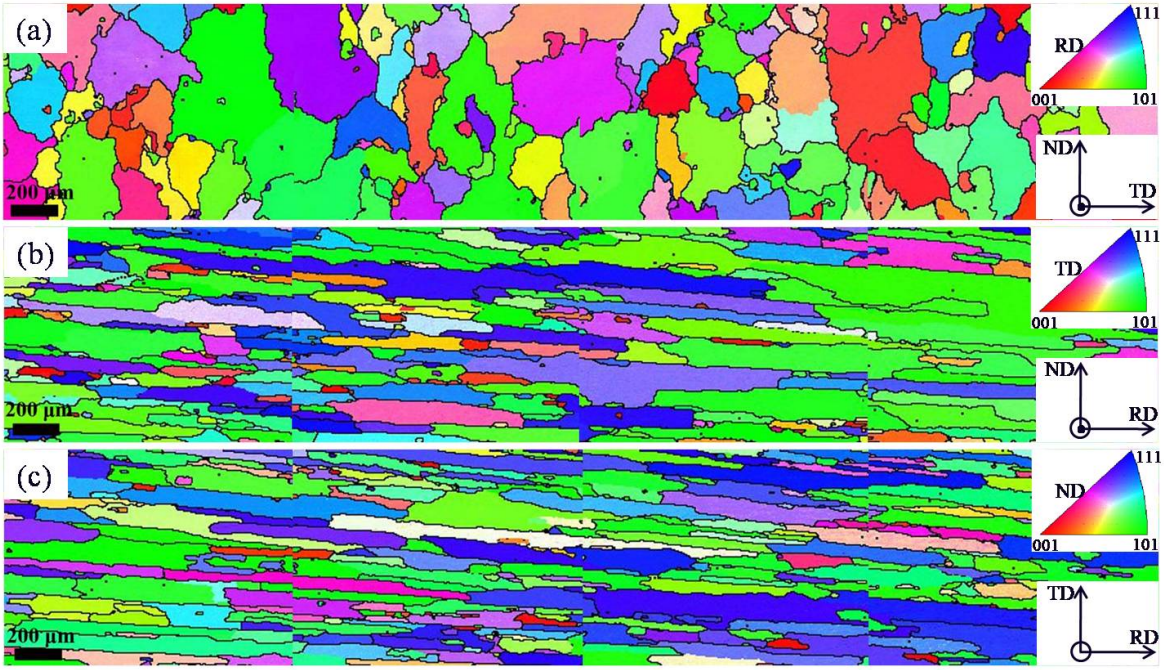

Fig. 4 EBSD IPF maps of as-received 6082-T6 Al sheet along different planes, (a) ND-TD, (b) ND-RD and (c) TD-RD.

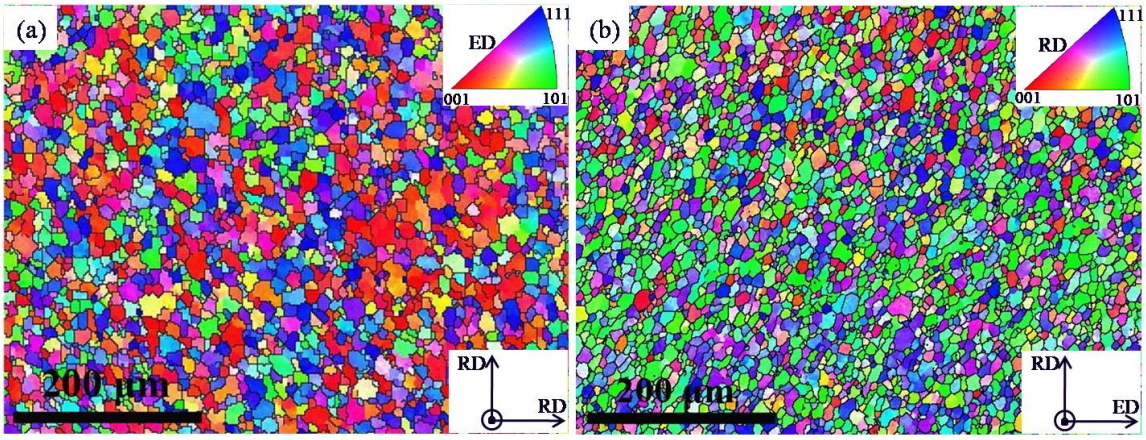

Fig. 5 EBSD IPF maps of the as-received CoreFlowed Al wire along different directions, (a) cross section and (b) longitudinal section.

3.3.2. Grain boundary

Fig. 6 shows grain boundaries (GBs) character, recrystallization distribution and the corresponding grain boundary misorientation of the as-received CoreFlowed Al specimen along the longitudinal section. As illustrated in Fig. 6a, a large number of low-angle grain boundaries (LAGBs) were introduced into the equiaxed grain in the as-received CoreFlowed Al specimen. It can be seen from the GBs map in Fig. 6a that the distribution of LAGBs in equiaxed grains is quite inhomogeneous, indicating that the grains with different orientations were subjected to different plastic deformation during CoreFlow^{TM} process due to a complex coupling of stress. Moreover, only a few Σ3 boundaries (0.714%) appear in CoreFlowed Al specimen, as shown in Fig. 6b. The appearance of a few annealing Σ3 twins is due to the medium stacking fault energy of the experimental Al-Mg-Si alloy with a FCC structure. The corresponding grain boundary misorientation distribution map in Fig. 6d shows the fraction of LAGBs up to 86.87%, which is attributed to heavy shear deformation and incomplete full recrystallization during CoreFlow^{TM} process. Zhang et.al [38] predicted that the maximum temperature at the center of the die/sample interface during friction extrusion process was ~ 823K, which would take ~ 10 seconds to reach the maximum temperature. Once the material is released from the die, the temperature will immediately drop to a low temperature. Since a tool rotational speed of 1200 rpm was used to prepare the CoreFlowed Al wire, the experience time is only ~ 10 seconds from the friction stirring to the CoreFlowed wire's extrusion. Hence, it is extimated that the CoreFlowed wire experienced a temperature gradient range of 273-823 K during the whole friction stirring process. As a result, partial LAGBs still remain in the CoreFlowed Al wire due to insufficient time migration and rearrangement at a low

temperature gradient.

The grain orientation spread (GOS) in EBSD has been frequently employed to distinguish the DRXed grains from the deformed parent grains [43]. Plastic deformation often results in a high GOS value in grains due to the distortion of grains, while the GOS value of recrystallised grains is low. In this study, a threshold value of 2^{o} is used for DRX of CoreFlowed Al, since the threshold value for GOS to separate the DRXed grains from the un-recrystallized ones varied between 1^{o} and 2^{o} in various materials [44, 45]. The GOS map of CoreFlowed Al specimen along the longitudinal section shown in Fig. 6c suggests that the volume fraction of DRXed grains is about 58.6% after processing of CoreFlow^{TM}. In other words, a large number of sub-structured and deformed grains remain in CoreFlowed Al specimen. After careful observation, it is found that the size of the deformed grains in the CoreFlowed Al wire (~ 50 μm) is much smaller than that in the as-received Al rolled sheet (~ 2000 μm), which may be caused by the re-deformation of the recrystallized grains formed in the early stage during CoreFlow^{TM} process.

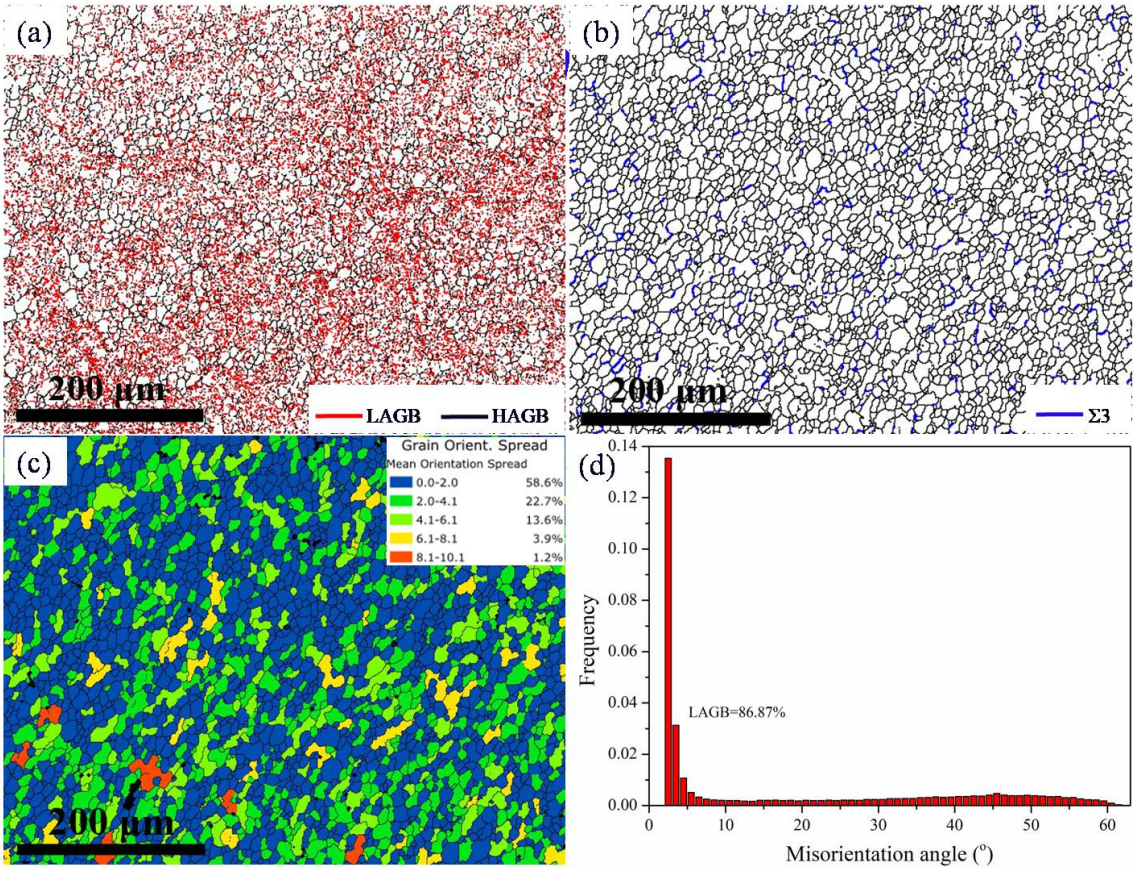

Fig. 6 Grain boundaries (GBs) character recrystallization distribution map of CoreFlowed Al specimen along longitudinal section. HAGBs plus LAGBs map (a), HAGBs plus Σ3 grain boundaries map (b), grain orientation spread (GOS) map (c), and the corresponding grain boundary misorientation distribution (d).

3.3.3. Micro-texture

Fig. 7 demonstrates the pole figures (PFs) of the initial 6082-T6 Al sheet and as-received CoreFlowed Al specimens. There is a random texture in the as-received Al sheet whether along the TD-RD or along the other two longitudinal sections (ND-RD/TD), as shown in Figs. 7a-c. It is worth noting that the random texture in the initial Al sheet with a maximum intensity of more than approximately 18.36 times above the random background is attributed to insufficient grain number statistics due to its coarse grains. After CoreFlow™ process, different amounts of texture components have been formed in

CoreFlowed Al wire, but only a few weak textures with a maximum intensity of less than about 4.85 times above the random background appear in CoreFlowed 6082 Al wire.

A tolerance of 15^{o} deviation from ideal texture components was considered in the EBSD maps. The common texture components of CoreFlowed Al wire were calculated by HKL-Channel 5 software, as shown in Fig. 8, and the corresponding content of each texture component is listed in Table 2. The texture components of as-received 6082 Al sheet is not listed in Table 2 owing to low statistics in Fig. 4. It is found from Table 2 that the dominant texture component is S {123}<634> (V=8.24%) along the cross-section, and Goss {110}<001> (V=6.86%) along the longitudinal section, respectively. The random grains with no preferred orientation still dominate in CoreFlowed Al specimen whether along the cross (V=82.76%) or longitudinal (V=82.84%) section. The comparison between the experimental {111} PF of S and Goss texture, the standard {111} PF of S and Goss texture, and the corresponding rotated {111} PF is shown in Fig. 7d-d_2 and 7e-e_2. It is found that the experimental {111} PF is in good agreement with the rotated {111} for both texture component S along cross section and texture component Goss along longitudinal section. Compared with the standard {111} PF of texture, the resulting texture in CoreFlowed Al is deflected by about 20^{o} counterclockwise (Figs. 7d_1, d_2, e_1, e_2), which may be related to the complex specific flow stress during CoreFlow^{TM}. Using a three-dimensional computational fluid dynamics model with consideration of both heat transfer and material flow shows that the material in the central region is pushed spirally upwards toward the extrusion hole to form the extrusion wire [17].

The evolution of the micro-texture is believed to be the result of the complex

material flow during CoreFlow^{TM} process. During the processing, the base material was firstly cut and extracted by the thread probe when it was rotating and moving forward. The materials were transported with the tool's rotation and welded together in a helical mode in the region where threads end. According to the structure of the rotational probe (Fig. 1a), the angle between the forward direction of CoreFlowed wire and the shearing force is approximately 45^{o} during the friction stir extrusion. If the orientation of a grain turns to the S-oriented during the severe thermal deformation, the corresponding Schmid factor of the grain is quite high (SF=0.478) among the grains with different orientations including Brass, Cube and Goss. Under the soft orientation, the {111}<110> slip system is easy to operate and thus can better coordinate the severe deformation of CoreFlowed wire during CoreFlow^{TM} process. On the other hand, the S-oriented grains are usually the "stable" orientation formed by the rotation of the cubic grains after "splitting" during plastic deformation. As a result, the dominant texture component is S {123}<634> (V=8.24% in Table 2) in the CoreFlowed Al wire along the cross-section.

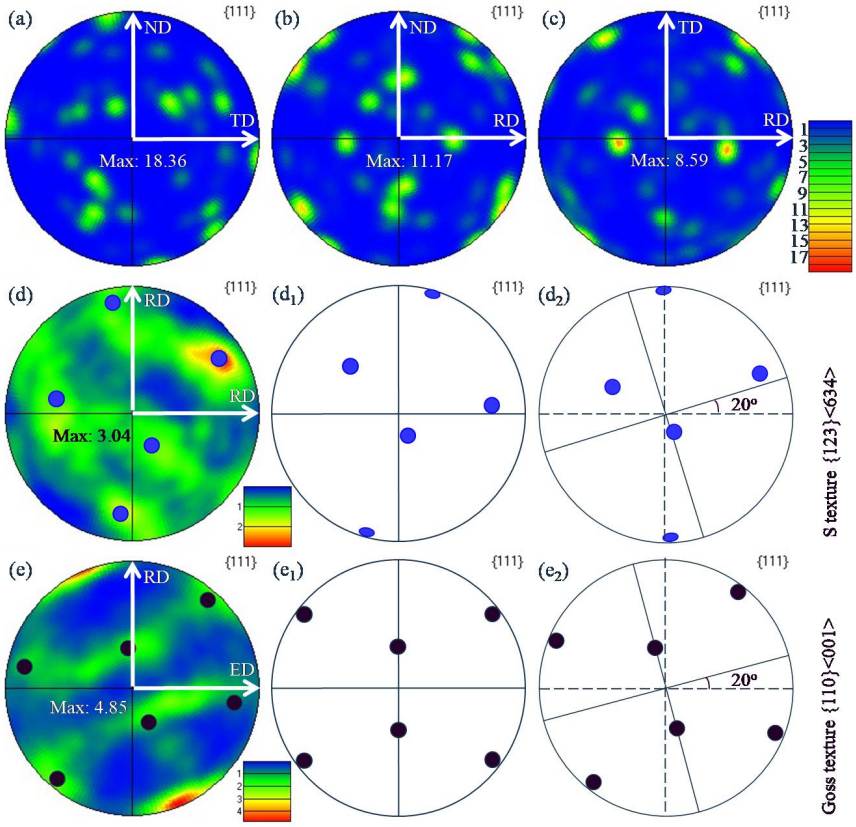

Fig. 7 EBSD {111} PF of as-received 6082-T6 Al sheet (a-c) along different planes and CoreFlowed Al wire along different directions (d, e), (d_1) and (e_1) showing the standard {111} PF of S and Goss texture, respectively, and the corresponding {111} PF obtained after 20^o counterclockwise rotate of standard {111} PF of S (d_2) and Goss texture (e_2).

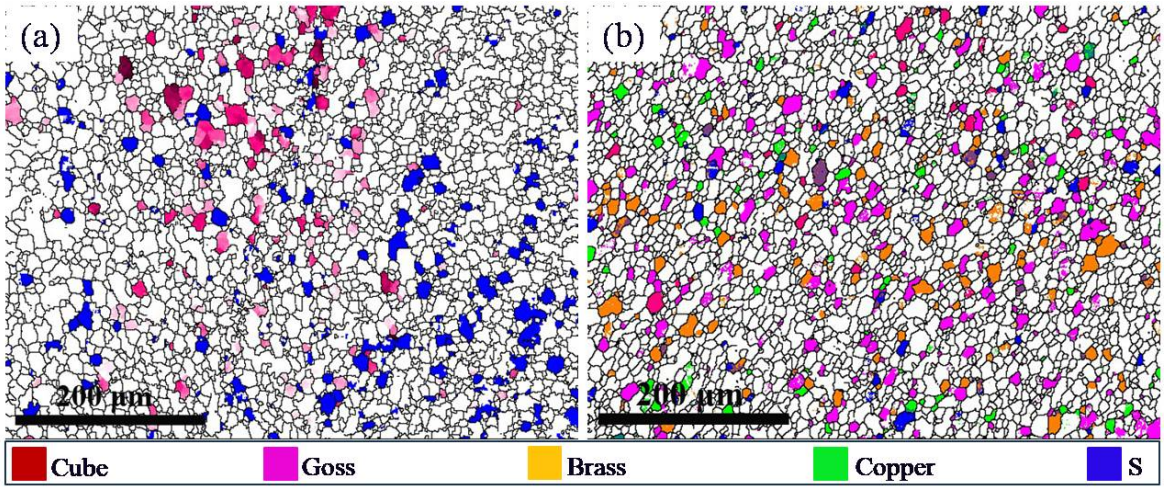

Fig. 8 Texture components of CoreFlowed Al wire along cross section (a) and longitudinal section (b).

Table 2 Micro-texture components (%) in the CoreFlowed Al wire

Direction	Brass {011}<211>	S {123}<634>	Copper {112}<111>	Goss {110}<001>	Cube {001}<100>	Bal.(Random)
Cross section	2.94	**8.24**	4.16	0.99	0.91	82.76
Longitudinal section	5.00	2.16	2.06	**6.86**	1.08	82.84

3.3.4. Feature of second phase particles

SEM images of the initial 6082-T6 Al alloy sheet and as-received CoreFlowed Al wire are shown in Fig. 9, which presents the strong tailor effect of CoreFlow™ process on distribution, size and morphology of second phase particles in parent 6082-T6 Al alloy. The secondary phase particles arranged in chain along the elongated grains (Figs. 9b, c), like-network distribution (Fig. 9a), and coarse particles (Fig. 9e) of the as-received Al sheet can be observed, which have been broken into uniformly distributed small particle phases in the CoreFlowed wires (Fig. 9d). The size of the dispersed homogeneously particle in Fig. 9f is significantly finer than in Fig. 9e, indicating that large particles were crushed into small ones under the shear stress and deformation heat during CoreFlow™. Meanwhile, the statistical data shows that the volume fraction of the secondary phases decreased from 6.2% in the as-received Al sheet to 4.9% after CoreFlow™. The results mentioned above indicate that the novel CoreFlow™ process plays a crucial role in the redistribution and refinement of original secondary phase particles.

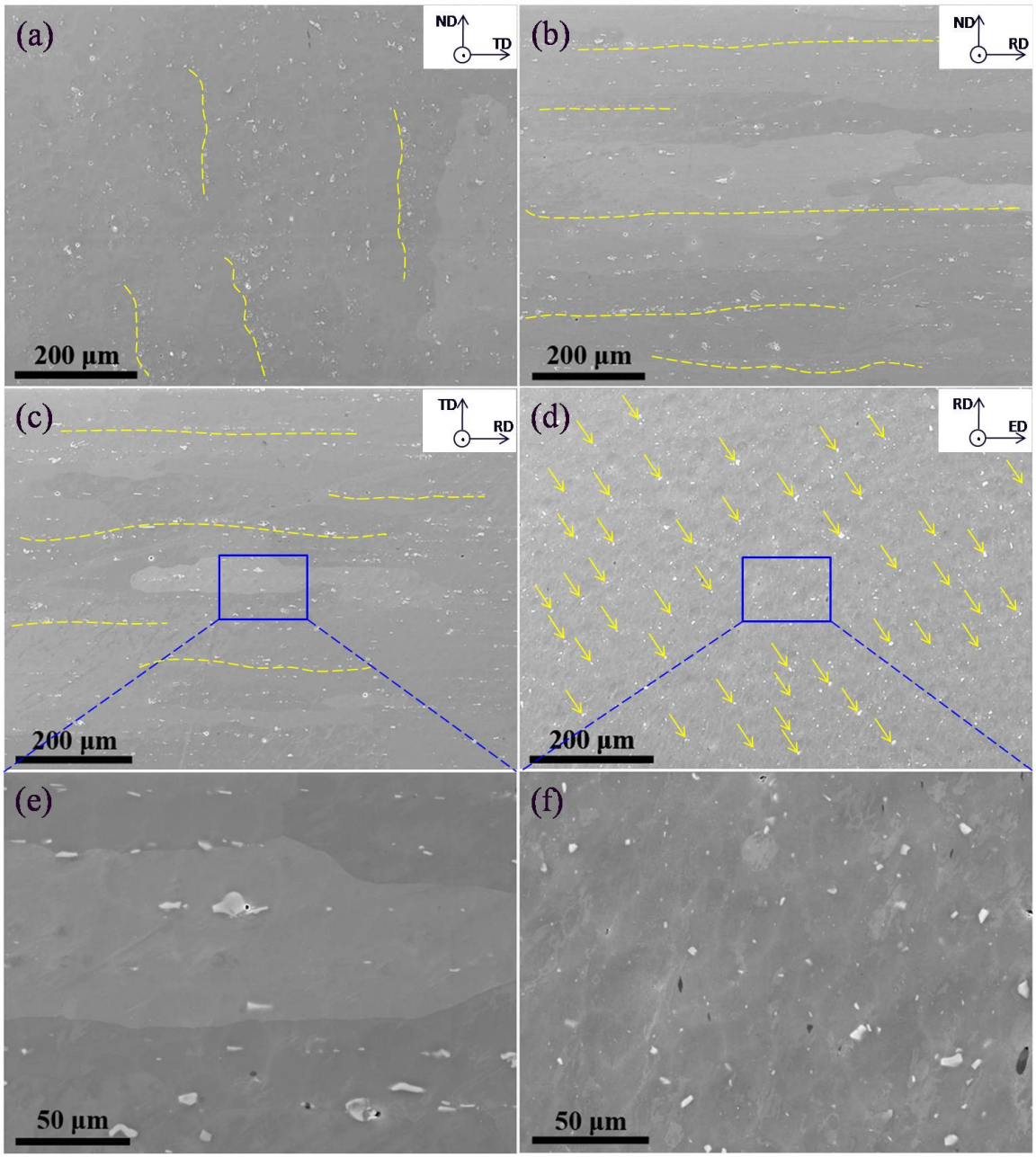

Fig. 9 SEM images of as-received 6082-T6 Al sheet (a-c, e) and as-received CoreFlowed Al wire (d, f) along different directions. (a) ND-TD, (b) ND-RD, (c) TD-RD, (d) longitudinal section, both (e) and (f) showing an enlarged version of the squared area in (c) and (d), respectively.

The severe stir-shear effect and frictions heat input during CoreFlow^{TM} result in recrystallization and grain refinement, as shown in Fig. 5. In fact, the uniformly-distributed secondary phase particles also contribute to recrystallization

through particle stimulated nucleation mechanism. Croteau et al. [15] reported that an attractive combination of yield strength (YS≈220 MPa) and elongation (>20%) exhibited in Al-Mg-Zr alloy processed shear-assisted processing extrusion. A similar strengthening effect was also recently reported by Li et al. [25] who observed an increase in YS (~43%) and compression strain (~36%) in FSEed Mg-RE alloy. The enhancement of mechanical properties after FSE was attributed to the effects: i) uniformly-distributed particle phases with fine sizes and ii) fine dynamic recrystallized grains. It is surmised that the desirable feature of secondary phase particles in CoreFlowed Al sample is responsible for good mechanical properties of CoreFlowed Al alloy. To determine the mechanical response of CoreFlowed Al specimen with the desirable feature of secondary phases, investigations on tensile properties of CoreFlowed Al specimens have been carried out at room temperature.

3.4. Mechanical performance

Tensile engineering and true stress-strain curves of the CoreFlowed specimens with different states are displayed in Fig. 10, together with those of the as-received 6082-T6 Al sheet specimen. The corresponding changes in the yield strength (YS, 0.2% offset stress), ultimate tensile strength (UTS) and elongation (EL) of the different specimens are summarized in Table 3. After CoreFlow^{TM} processing, the average grain size decreases sharply up to ~7.6 μm (Fig. 5), while the change of mechanical behaviour of the as-received CoreFlowed Al specimen does not follow the classical Hall-Petch relationship. The elongation of the as-received CoreFlowed Al specimen reached 19.3%, which was more than around 100% higher than that of the as-received 6082-T6 Al sheet (10.4%),

while its YS value still remains an acceptable value (YS=182 MPa), which resulted in a good strength-ductility synergy in fine-grained CoreFlowed Al specimen. Moreover, the calculation result shows that the fracture toughness of the as-received CoreFlowed Al specimen (3.36 KJ/m^2) is much higher than that of the as-received Al sheet (2.01 KJ/m^2). After ageing via a simple one-step treatment at 175 ^oC for 10 h, the YS value of the aged CoreFlowed Al specimen increases sharply to 254 MPa while only maintaining 9% elongation. The result suggested that different deformation modes took place in CoreFlowed Al specimens with different states during plastic deformation.

Due to the higher work hardening capability ($d\sigma_T/d\varepsilon_T$) of the as-received CoreFlowed Al specimen, the final UTS of CoreFlowed Al specimen climbed to 316.8 MPa in the true stress-strain curve, which almost is the same level as the as-received 6082-T6 Al sheet (UTS=324.6 MPa), as shown in Fig. 10a. However, the final UTS of aged CoreFlowed Al specimen is lower than that of the as-received Al sheet and CoreFlowed Al specimen due to the lower work hardening capability ($d\sigma_T/d\varepsilon_T$).

It is known that the strain hardening rate (θ) significantly affects the uniform elongation according to the plastic instability condition, and necking takes place when $\theta<\sigma_T$ [46]. The strain hardening rates as a function of true strains are compared in specimens with different states, as shown in Fig. 10b. For the coarse-grained 6082-T6 Al sheet specimen, the strain hardening rate decreased with increasing strain at an initial stage, corresponding to the plastic deformation initiated by dislocation glides, which was consistent with those of alloys with same crystal structure and similar grain sizes [47]. When the true strain reached 0.035, the decrease of strain hardening rate slowed down,

suggesting the appearance of sub-structures which provided interfacial barriers for dislocation movement to enhance dislocation accumulation [48].

Since a large number of LAGBs remain in grains of the as-received CoreFlowed Al specimen (Fig. 6a), the LAGBs in the aged CoreFlowed Al specimen will be further rearranged and relaxed in atomic scale after ageing at 175 ^{o}C for 10h. Hence, regarding aged CoreFlowed Al specimen, the lower dislocation density in the initial straining process led to lower strain hardening rate, and then significantly recovered to a high value until the strain reached 0.065.

The as-received CoreFlowed Al specimen showed a complicated strain hardening behavior, which was extraordinarily different from the aged CoreFlowed Al and 6082-T6 Al specimen. There are five distinct hardening stages (I-V) in as-received CoreFlowed Al wire based on the changes of the strain hardening rate, indicating that different deformation mechanisms may occur in different deformation stages. The initial rapid drop of work hardening corresponding to stage I (ε_T=0-3.6%) indicates the start of plastic deformation after yielding. Upon straining to stage II (ε_T=3.6-6.6%), the work hardening rate increases slowly to maximum values of 2.25 GPa at ~6.6% strain. With further straining to stage III (ε_T=6.6-11%), the work hardening rates drop to 0.2 GPa. In stage IV (ε_T=11-14%), the work hardening rate increases slowly to 1.4 GPa again. In stage V (ε_T=14-16%), the work hardening rate decreases gradually, leading to fracture at 0.151 strain.

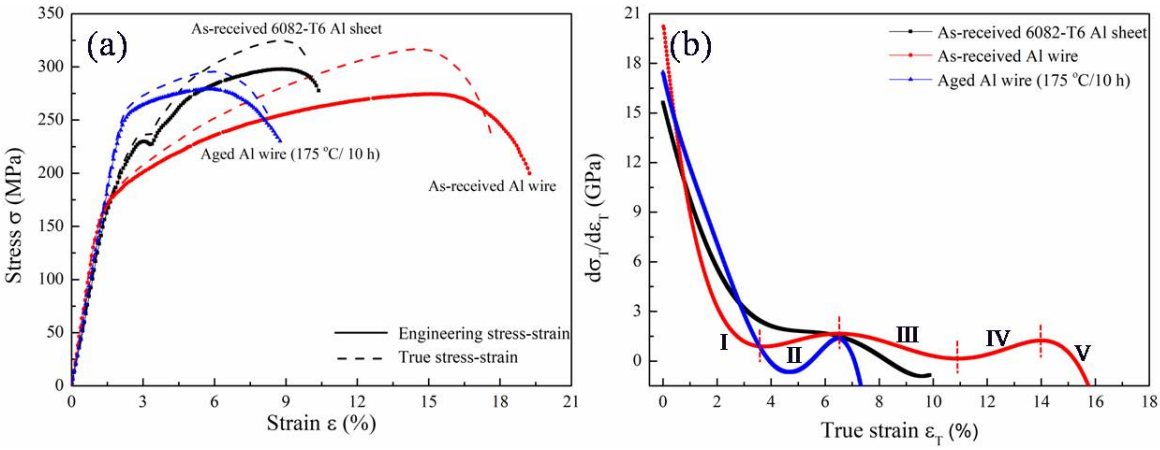

Fig. 10 Mechanical properties of the different samples, (a) tensile engineering and true stress-strain curves, and (b) the corresponding strain hardening rate curves against the true strain.

Table 3 Tensile mechanical properties of the different samples at room temperature

Sample	Yield strength YS (MPa)	Ultimate tensile strength UTS (MPa)	Elongation EL(%)
As-received 6082-T6 Al sheet	225	297.8/324.6*	10.4/9.9*
As-received CoreFlowed Al wire	182	275.4/316.8*	19.3/17.6*
Aged Al wire (175 °C/10 h)	250	278.2/296.8*	9.0/8.4*

Noted that asterisks represent properties obtained via true stress-strain curve

It has been verified [49] that *Zener-Holloman* parameter $Z=\varepsilon\exp(Q/RT)$ combined of the working temperature and strain rate has been used to predict the resulting grain size in extruded alloys (where ε is the strain rate, R is the gas constant, T is the temperature, and Q is the related activation energy). The calculated grain size of the CoreFlowed Al specimen is about 8 μm based on the relationship of $\ln d=9.0-0.27\ln Z$ derived by Chang et al. [49] from FSEed alloy, which is consistent with EBSD results in Fig. 5.

The refined grain does not increase the yield strength (Fig. 10a) of CoreFlowed Al specimen compared to coarse grained 6082-T6 Al sheet. In other words, CoreFlow™ process tends to soften the alloys in the present study, even though the grain is

significantly refined. It is known that the precipitate hardening in the heat-treatable Al alloys of 6xxx series is the main strengthening mechanism [28, 29], especially, the precipitation of the metastable β''-Mg_2Si precipitates determines the dispersion hardening of the heat-treatable Al alloys. However, the redissolution and coarsening of the strengthening phases occurred in CoreFlowed Al wire due to the high heat of friction stir input during CoreFlow™ process, as shown in Fig. 3. Therefore, the mechanical properties of as-received CoreFlowed Al wire exhibit softening phenomenon, although its grain size was severely refined. Kurabayashi et al. [50] found that the hardness was mainly affected by precipitation hardening, but not refined grains after friction stir welds.

3.5. Deformation behaviour

3.5.1. Fracture morphology

To analyze the fracture mechanism, the scanning electron fractograph of tensile specimens has been observed in the as-received 6082-T6 Al alloy sheet, as-received CoreFlowed Al, and aged CoreFlowed Al. The SEM fractography of tensile fractures in the surface region of three kinds of samples was shown in Fig. 11. It can be seen that the failure mode in three kinds of samples display a “cup-cone” type of fracture, and three zones including fibrous, radial and shear lip, can be observed. These features combined with a necking phenomenon and tearing ridges indicate that the fracture mode of three kinds of samples is all a typical ductile fracture. Compared to that in 6082-T6 Al sheet and aged CoreFlowed Al specimen, the fibrous zone in as-received CoreFlowed Al specimen is relatively smaller, as marked by the dashed ellipses in Fig. 11a_1-c_1, which indicates that it has better ductility, which is consistent with high ductility of as-received CoreFlowed Al

specimen in Fig. 10a and Table 3.

Although the fibrous region of the three kinds of samples is composed of a large number of dimples, the dimples in as-received CoreFlowed Al specimen are relatively deep compared with that in 6082-T6 Al sheet and aged CoreFlowed Al. The formation of the dimples was initiated by the second phase particles by nucleating voids and micro-pores under increasing load. These particles could be observed inside the dimples on the fracture surface, as shown in Fig. 11a_3-c_3. The uniform distribution of relatively small particles provided the formation of equiaxed dimples in equivalent size, while the large particles resulted in the discontinuous fracture of the dimples and formation of quasi-cleavage facets (inset in Fig. 11c_2) that can reduce the ductility of the material. Moreover, it is found that there were many micro-cracks (marked by the green arrows in Fig. 11c_2) around the hard particles in the aged CoreFlowed Al specimen, which is an important factor for the reduced ductility of the aged CoreFlowed Al specimen compared to as-received CoreFlowed Al wire.

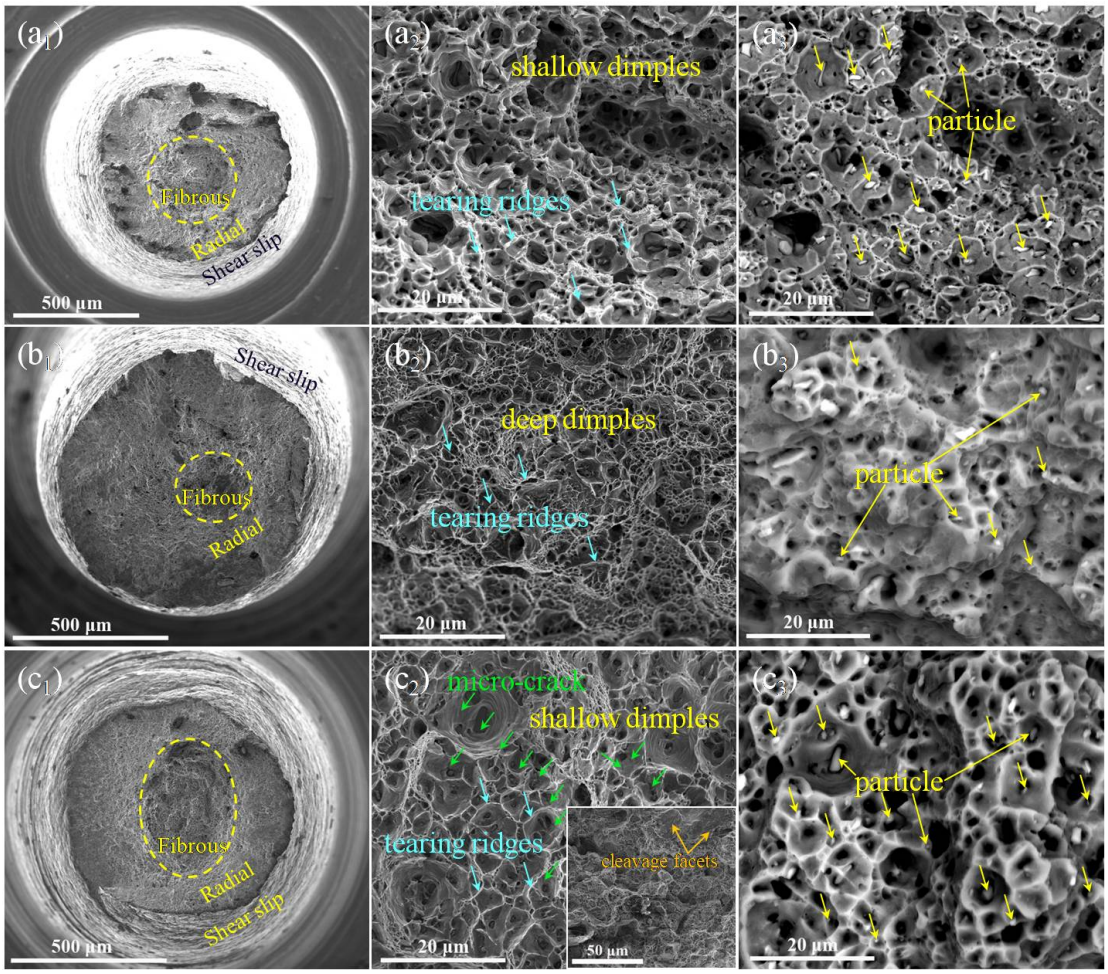

Fig. 11 SEM micrographs of the tensile fracture of the different specimens, (a_1-a_3) as-received 6082-T6 Al sheet, (b_1-b_3) as-received CoreFlowed Al wire, and (c_1-c_3) aged CoreFlowed Al wire; (a_1-c_1) low magnification of the fracture, (a_2-c_2) high magnification, (a_3-c_3) SEM-BSE image of the fracture. Inset in c_2 showing cleavage facets and "rock candy" morphology.

3.5.2. EBSD characterization near fracture surface

To understand underlying deformation mechanisms, the representative specimens were selected from region *b* (1 mm to the fracture point) in Fig. 12a for characterizing deformation microstructures after tensile deformation to failure. In addition, a counterpart region *c* away from the fracture (~7 mm) was also characterized for a

comparison test. Equiaxed grains could be still observed even after experiencing such a major tensile strain of 19.3%, and the average grain size remained almost constant (d=8 μm, in Fig. 12b) when compared to as-received CoreFlowed Al wire (d=7.4 μm) and a counterpart region *c* (d=7.8 μm, in Fig. 12c). It can be seen from Fig. 12d that the distribution of LAGBs in some grains is still mainly concentrated around HAGBs after tensile deformation, and LAGBs density within equiaxed grains seemed low compared to as-received CoreFlowed Al wire in Fig. 6d. These microstructure features indicated that grain-boundary sliding (GBS) is also involved in deformation mode in the as-received CoreFlowed Al wire during tensile at room temperature in addition to the dislocation slip.

Fig. 13b shows that the Schmid factor (SF) image of the deformed CoreFlowed Al sample with an FCC structure under slip systems {111}<110> was distributed over a wide range from 0.3 to 0.5. In other words, the corresponding crystal changes from hard orientation to soft orientation, which led to the inhomogeneity of the plastic deformation between hard-oriented grain and soft-oriented grain following the Schmid's law. As a result, the GBS mechanism that participates in plastic deformation is activated in deformed CoreFlowed Al wire in order to alleviate the strain incompatibility, since the strain incompatibility is an induction factor for the occurrence of the GBS mode [37, 51]. Moreover, the occurrence of the GBS mechanism becomes easier in a fine-grained CoreFlowed Al wire (Fig. 5), which is consistent with the generally accepted view that the tendency of GBS increases with decreasing grain size [52]. By associating the KAM diagram of an individual grain with its corresponding SF value, as marked by the white dotted line in Figs. 13a and b, it can be found that the KAM image of the individual grain

with a large SF value is unevenly distributed, i.e., a low KAM value in grains and a high KAM value along the grain boundary, indicating the activation of the GBS mechanism during plastic deformation. Take a single grain (G_1 and G_2) in Fig. 13a for example, the KAM difference (ΔKAM) between along the grain boundary (GB_{KAM}) and within the grain (GI_{KAM}) in G1 is much higher than that of G2, as shown in Fig. 13c, which further indicated that the GBS mechanism was activated in some grains during deformation. If the high KAM value along the GBs is only caused by the hindering effect of grain boundaries on dislocations, the ΔKAM in the G1 will not be much higher than that in G2.

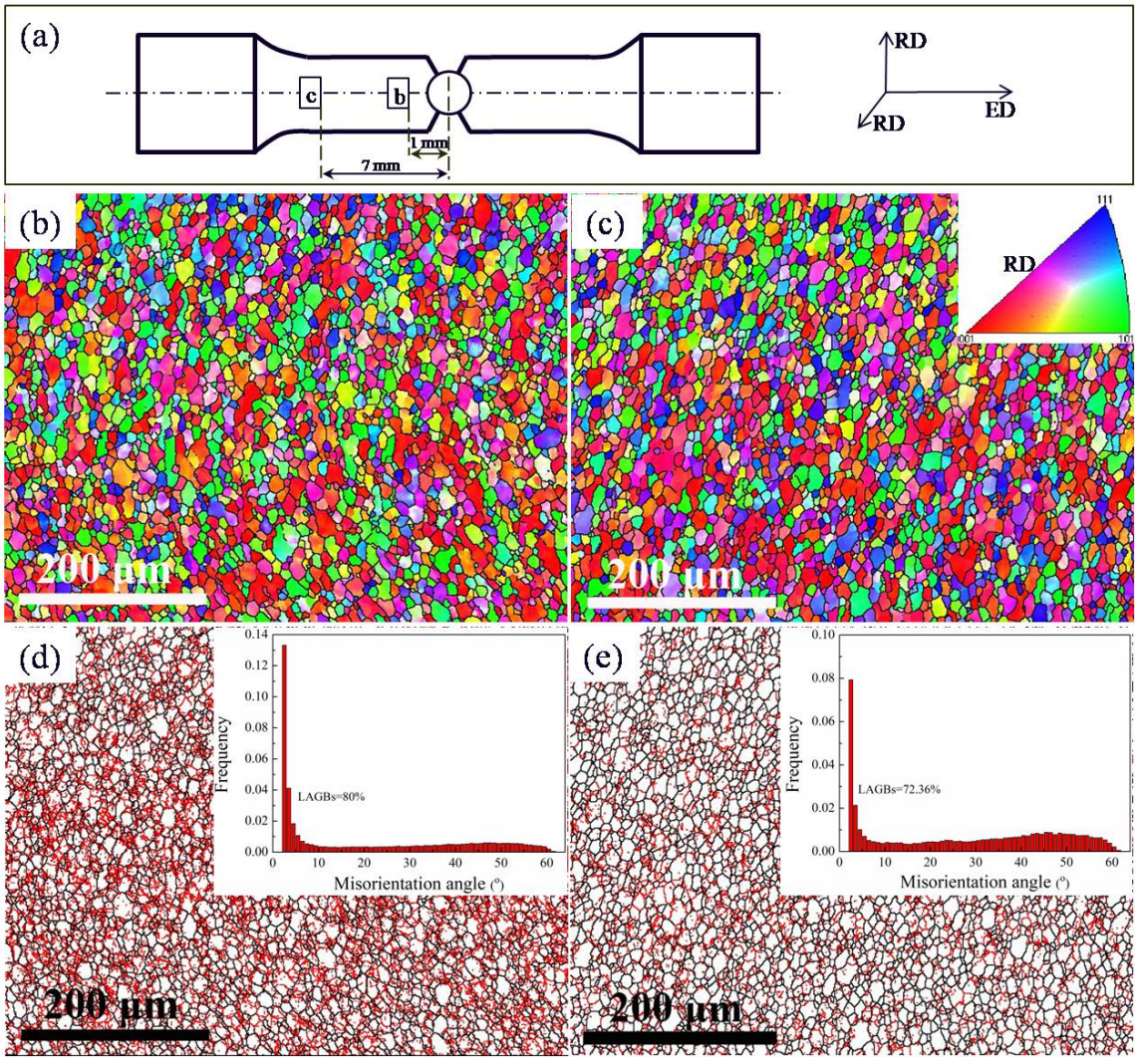

Fig. 12 The locations of the EBSD map of post-fracture samples (a), EBSD-IPF mapping of

the rectangles in b region (b) and c region (c) in (a), respectively, the corresponding EBSD-GBs mapping of (b) image (d) and (c) image (e). Inset in (d) and (e) showing the corresponding grain boundary misorientation distribution.

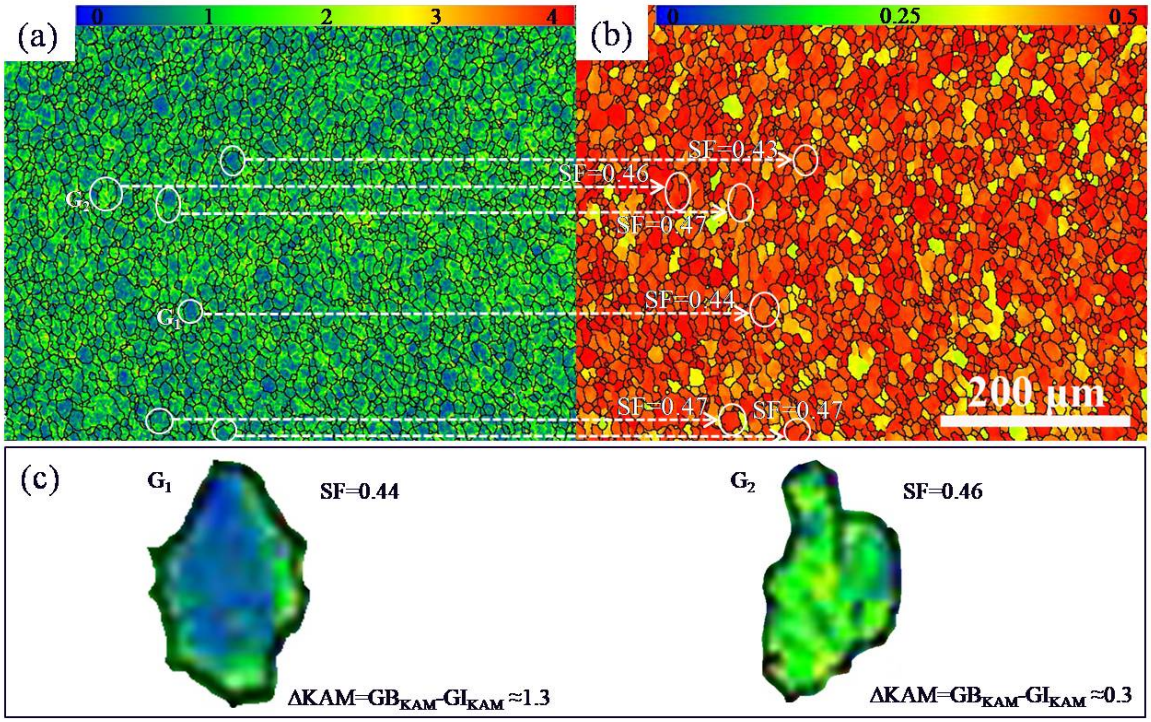

Fig. 13 Corresponding KAM image (a) and SF image (b) of Fig. 12b, magnified view (c) of typical grain marked by G_1 and G_2 in (a).

3.5.3. Deformation mechanism

The schematic illustrating the deformation mechanism of Al alloy with different states at room temperature is presented in Fig. 14. Due to the appearance of precipitation phases in the alloy matrix after ageing via T6, precipitate strengthening is mainly responsible for high yield strength of coarse-grained 6082-T6 Al alloy sheet, as shown in Fig. 10a. After processing of CoreFlow^{TM}, four remarkable things happened in CoreFlowed Al wire: i) grain refinement (~ 8 μm in diameter) (Fig. 5); ii) redistribution and fragmentation of original second phase particles (Fig. 9d, and 9f); iii) redissolution of

original fine precipitates; iv) appearance of equiaxed grain with different deformation abilities (Fig. 6c). As a result, the contribution of precipitate strengthening decreased significantly, while the grain boundary strengthening was weaker than precipitation strengthening in Al alloys. Moreover, the occurrence of the GBS further weakened the grain boundary strengthening effect. However, it has been reported that fine grain size was then considered effective for enhancing the compatibility effect [2, 53]. Therefore, the as-received CoreFlowed Al wire exhibit excellent ductility (EI=19.3%) and acceptable yield strength (YS=182 MPa). After ageing treatment at 175 ^{o}C for 10h, new nanoscale precipitates were reformed. Certainly, some original fine-strengthening precipitates after CoreFlow^{TM} processing were either subject to phase growth or phase transformation, which would partially reduce the strength of the material. However, calculating the exact amount of strength improvement introduced by newly reformed fine precipitates and strength loss caused by the growth/transformation of initial precipitates requires another detailed analysis and will be reported in another paper. In this case, based on the results of Table 3, the combination of newly formed precipitate strengthening and grain boundary strengthening based on dislocation pileups at grain boundaries outweighed the strength loss caused by the growth/evolution of the original precipitate after CoreFlow^{TM} processing, leading to a sharp increment of yield strength in aged CoreFlowed Al wire. Meanwhile, the coarse particle phases distributed along the grain boundaries or in grains became the source of micro-cracks initiation (Fig. 11c$_2$), resulting in a significant decrease in ductility. To further improve the strength and ductility of the as-received CoreFlowed wires simultaneously, an optimized heat treatment procedure needs to be identified in

our future work, which will largely expand the Al wire applications where high toughness is required.

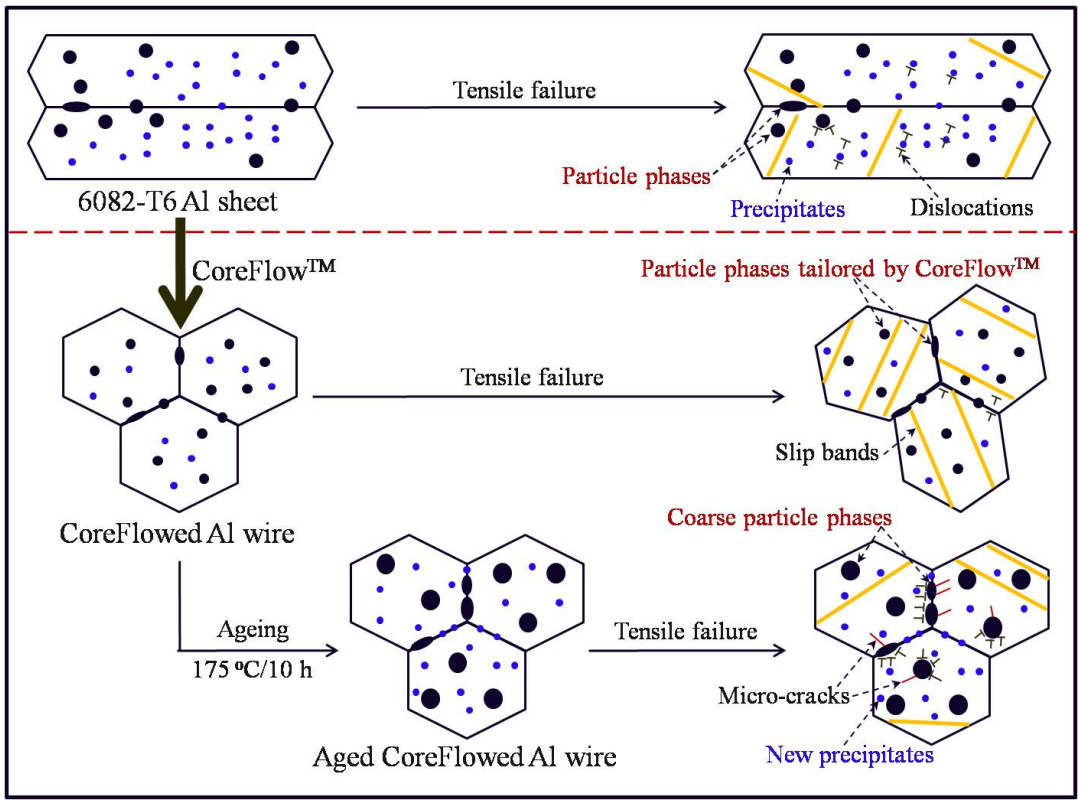

Fig. 14 Schematic illustration of deformation mechanism for the Al alloys with different states including 6082-T6 Al sheet, CoreFlowed Al wire and aged CoreFlowed Al wire.

4. Conclusions

In this work, a novel severe plastic deformation (SPD) method, which is bulk-consolidation friction stir extrusion enabled by CoreFlow™ process based on the friction stir extrusion of alloy sheet, is utilized to fabricate 6082 Al alloy wires with excellent mechanical properties in a single step at room temperature, thereby dramatically reducing the production cost if this process is commercialised. The microstructure evolution, secondary phase particles behaviour and mechanical response of CoreFlowed 6082 Al wires was characterized and investigated via XRD, EBSD, Vickers

hardness, and room temperature X-ray computed tomography (XCT). The following conclusions can be drawn:

1) After processing of CoreFlow^{TM}, the grain of alloy material was sharply refined of about 200-fold from ~2000 μm of initial 6082 Al alloy sheet to ~10 μm of yielding Al wire, which is rare in other SPD methods for processing alloy wires. In addition, a high density of low angle grain boundaries appeared in the equiaxed grain obtained during CoreFlow^{TM} process, indicating the inadequacy of dynamic recrystallization. Meanwhile, the overall micro-texture intensity of CoreFlowed Al wire is weak, despite including a few texture components of S (V=8.24%) and Goss (V=6.86%).

2) The undesirable feature of a coarse and preferred secondary phase particles in initial 6082-T6 Al sheet was well tailored by CoreFlow^{TM} process, leading to an attractive characteristic of dispersed and refined second phase particles in CoreFlowed Al wires. Owing to the synergy effect consisting of friction heat and stir shear force during the friction stir extrusion, dissolution and fragmentation of the partial strengthening precipitates occur in CoreFlowed Al wire, which led to a decrease in hardness and tensile strength at room temperature.

3) Compared to the initial 6082-T6 Al sheet (EI=10.4%, and YS=225 MPa), CoreFlowed Al wire had excellent ductility (EI=19.3%) and an acceptable yield strength (YS=182 MPa) due to a cooperative deformation modes composing of dislocation slip and grain boundary sliding. Benefiting from the higher work hardening capability, the final ultimate tensile strength (UTS=316.8 MPa) of the as-received CoreFlowed Al wire reached almost the same level as the 6082-T6 Al sheet (UTS=324.6 MPa). Meanwhile, a simple

one-step ageing heat treatment at 175 ^{o}C for 10 h rapidly improved the YS of aged CoreFlowed Al wire to 254 MPa while still maintaining 9% elongation, which could be attributed to the synergy effect of precipitate strengthening and Hall-Petch strengthening.

Declaration of competing interest

The authors declare that they have no known competing financial interests or personal relationships that could have appeared to influence the work reported in this paper.

Acknowledgements

The authors gratefully acknowledge funding through UKRI MRC Future Leaders Fellowship (No. MR/T019123/1). L.Y. would like to thank China Scholarship Council (CSC) for the award of fellowship (No. 201908610075).

Data availability

The raw/processed data required to reproduce these findings cannot be shared at this time as the data also forms part of an ongoing study.

References

[1] Z.Y. Ma, F.C. Liu, R.S. Mishra, Superplastic deformation mechanism of an ultrafine-grained aluminum alloy produced by friction stir processing, Acta Mater. 58 (2010) 4693-4704.

[2] R.X. Zheng, J.P. Du, S. Gao, H. Somekawa, S. Ogata, N. Tsuji, Transition of dominant deformation mode in bulk polycrystalline pure Mg by ultra-grain refinement down to sub-micrometer, Acta Mater. 198 (2020) 35-46.

[3] K. Majchrowicz, Z. Pakiela, W. Chrominski, M. Kulczyk, Enhanced strength and electrical conductivity of ultrafine-grained Al-Mg-Si alloy processed by hydrostatic extrusion, Mater. Charact. 135 (2018) 104-114.

[4] E. Ma, T. Zhu, Towards strength-ductility synergy through the design of heterogeneous nanostructures in metals, Mater. Today 20 (2017) 323-331.

[5] C.S. Lei, X.L. Li, X.T. Deng, Z.D. Wang, G.D. Wang, Deformation mechanism and ductile fracture behavior in high strength high ductility nano/ultrafine grained Fe-17Cr-6Ni austenitic steel, Mater. Sci. Eng. A 709 (2018) 72-81.

[6] W.C. Ke, J.P. Oliveira, S.S. Ao, F.B. Teshome, L. Chen, B. Peng, Z. Zeng, Thermal process and material flow during dissimilar double-sided friction stir spot welding of AZ31/ZK60 magnesium alloys, J Mater. Res. Tech. 17 (2022) 1942-1954.

[7] A.M.S. Costa, J.P. Oliveira, V.F. Pereira, C.A. Nunes, A.J. Ramirez, A.P. Tschiptschin, Ni-based Mar-M247 superalloy as a friction stir processing tool, J Mater. Process. Tech. 262 (2018) 605-614.

[8] J.P. Oliveira, J.F. Duarte, P. Inácio, N. Schell, R.M. Miranda, T.G. Santos, Production of Al/NiTi composites by friction stir welding assisted by electrical current, Mater. Des. 113 (2017) 311-318.

[9] F. Pixner, R. Buzolin, F. Warchomicka, A. Pilz, N. Enzinger, Wire-based electron beam additive manufacturing of tungsten, Int. J. Refrac. Met. Hard Mater. 108 (2022) 105917.

[10] J.W. Elmer, G. Gibbs, Mechanical rolling and annealing of wire-arc additively manufactured stainless steel plates, Sci. Technol. Weld. Joining 27 (2022) 14-21.

[11] P.S. Guo, F.X. Li, L.J. Yang, R. Bagheri, Q.K. Zhang, B.Q. Li, K. Cho, Z.L. Song, W.S. Sun, H.N. Liu, Ultra-fine-grained Zn-0.5Mn alloy processed by multi-pass hot extrusion: grain refinement mechanism and room-temperature superplasticity, Mater. Sci. Eng. A 748 (2019) 262-266.

[12] S.J. Yuan, W.J. Cheng, W. Liu, Y.C. Xu, A novel deep drawing process for aluminum alloy sheets at cryogenic temperatures, J. Mater. Process. Technol. 284 (2020) 116743.

[13] M. Gao, I.P. Etim, K. Yang, L.L. Tan, Z. Ma, Enhancing mechanical property and corrosion resistance of Mg-Zn-Nd alloy wire by a combination of SPD techniques, extrusion and hot drawing, Mater. Sci. Eng. A 829 (2022) 142058.

[14] A.M. Jarrell, A.M. Strauss, Applying torque based control to friction stir extrusion, J. Manuf. Process. 80 (2022) 382-396.

[15] J.R. Croteau, J.G. Jung, S.A. Whalen, J. Darsell, A. Mello, D. Holstine, K. Lay, M. Hansen, D.C. Dunand, N.Q. Vo, Ultrafine-grained Al-Mg-Zr alloy processed by shear-assisted extrusion with high thermal stability, Scr. Mater. 186 (2020) 326-330.

[16] F. Abu-Farha, A preliminary study on the feasibility of friction stir back extrusion, Scr. Mater. 66 (2012) 615-618.

[17] H. Zhang, X. Li, X. Deng, A.P. Reynolds, M.A. Sutton, Numerical simulation of friction extrusion process, J. Mater. Process. Technol. 253 (2018) 17-26.

[18] X. Li, W. Tang, A.P. Reynolds, W.A. Tayon, C.A. Brice, Strain and texture in friction extrusion of aluminum wire, J. Mater. Process. Technol. 229 (2016) 191-198.

[19] W. Tang, A.P. Reynolds, Production of wire via friction extrusion of aluminum alloy

machining chips, J. Mater. Process. Technol. 210 (2010) 2231-2237.

[20] K. Tahmasbi, M. Mahmoodi, H. Tavakoli, Corrosion resistence of aluminum alloy AA7022 wire fabricated by friction stir extrusion, Trans. Nonferrous Met. Soc. China 29 (2019) 1601-1609.

[21] M. Sharifzadeh, M.A. Ansari, M. Narvan, Evaluation of wear and corrosion resistance of pure Mg wire produced by friction stir extrusion, Trans. Nonferrous Met. Soc. China 25 (2015) 1847-1855.

[22] V.C. Shunmugasamy, E. Khalid, B. Mansoor, Friction stir extrusion of ultra-thin wall biodegradable magnesium alloy tubes-microctructure and corrosion response, Mater. Today Commun. 26 (2021) 102129.

[23] D. Baffari, G. Buffa, D. Campanella, L. Fratini, Al-SiC metal matrix composite production through friction stir extrusion of aluminum chips, Procedia Eng. 207 (2017) 419-424.

[24] G. Jamali, S. Nourouzi, R. Jamaati, FSBE process: a technique for fabrication of aluminum wire with randomly oriented fine grains, Mater. Lett. 241 (2019) 68-71.

[25] J.C. Li, X.C. Meng, Y.L. Li, L. Wan, Y.X. Huang, Friction stir extrusion for fabricating Mg-RE alloys with high strength and ductility, Mater. Lett. 289 (2021) 129414.

[26] A.M. Jamili, A. Zarei-Hanzaki, H.R. Abedi, P. Minárik, R. Soltani, The microstructure, texture, and room temperature mechanical properties of friction stir processed Mg-Y-Nd alloy, Mater. Sci. Eng. A 690 (2017) 244-253.

[27] H. Shahsa, A. Zarei-Hanzaki, A. Barabi, J.H. Cho, Sang-Ho. Han, Dynamic dissolution and transformation of LPSO phase during thermomechanical processing of a GWZ

magnesium alloy, Mater. Sci. Eng. A 754 (2019) 85-98.

[28] Z.J. Cui, H.C. Jiang, D. Zhang, Y.Y. Song, D.S. Yan, L.J. Rong, Influence of Mn on the negative natural aging effect in 6082 Al alloy, Mater. Sci. Eng. A 793 (2020) 139874.

[29] M.X. Guo, J.Q. Du, C.H. Zheng, J.S. Zhang, L.Z. Zhuang, Influence of Zn contents on precipitation and corrosion of Al-Mg-Si-Cu-Zn alloys for automotive applications, J. Alloys Compd. 778 (2019) 256-270.

[30] Q.Y. Zhu, L.J. Chen, X.R. Huo, Influence of minor Sc addition on microstructure and mechanical properties of extruded Al-7Zn-2Mg-1.5Cu-0.1Zr alloy in T6 heat treatment, Mater. Trans. 60 (2019) 944-949.

[31] V. Fallah, B. Langelier, N. Ofori-Opoku, B. Raeisinia, N. Provatas, S. Esmaeili, Cluster evolution mechanisms during aging in Al-Mg-Si alloys, Acta Mater. 103 (2016) 290-300.

[32] A. Kalinenko, K. Kim, I. Vysotskiy, I. Zuiko, S. Malopheyev, S. Mironov, R. Kaibyshev, Microstructure-strength relationship in friction-stir welded 6061-T6 aluminum alloy, Mater. Sci. Eng. A 793 (2020) 139858.

[33] J. Hu, Y.N. Shi, X. Sauvage, G. Sha, K. Lu, Grain boundary stability governs hardening and softening in extremely fine nanograined metals, Science 355 (2017) 1292-1296.

[34] Z.M. Liang, X. Wang, C.W. Cai, D.L. Wang, Microstructure and mechanical properties of thick plate friction stir welds for 6082-T6 aluminum alloy, High Temp. Mater. Proc. 38 (2019) 525-532.

[35] A. Naumov, I. Morozova, E. Rylkov, A. Obrosov, F. Isupov, V. Michailov, A. Rudskoy, Metallugical and mechanical characterization of high-speed friction stir welded AA

6082-T6 aluminum alloy, Mater. 12 (2019) 4211.

[36] J.H. Peng, Z. Zhang, J.A. Huang, P. Guo, Y.Z. Li, W. Zhou, Y.C. Wu, The effect of the inhomogeneous microstructure and texture on the mechanical properties of AZ31 Mg alloys processed by friction stir processing, J. Alloys Compd. 792 (2019) 16-24.

[37] D. Ando, Y. Sutou, J. Koike, Internal microstructure observation of enhanced grain-boundary sliding at room temperature in AZ31 magnesium alloy, Mater. Sci. Eng. A 666 (2016) 94-99.

[38] H. Zhang, X. Li, W. Tang, X. Deng, A.P. Reynolds, M.A. Sutton, Heat transfer modeling of the friction extrusion process, J Mater. Process. Tech. 221 (2015) 21-30.

[39] N. Kumar, G.M. Owolabi, R. Jayaganthan, G. Warner, Effect of annealing on mechanical properties and metallurgical factors of ultrafine-grained 6082 Al alloy, Trans. Indian. Inst. Met. 72 (2019) 2523-2531.

[40] K. Tahmasbi, M. Mahmoodi, Evaluation of microstructure and mechanical properties of aluminum AA7022 produced by friction stir extrusion, J. Manuf. Process. 32 (2018) 151-159.

[41] W.T. Evans, B.T. Gibson, J.T. Reynolds, A.M. Strauss, G.E. Cook, Friction stir extrusion: a new process for joining dissimilar materials, Manuf. Lett. 5 (2015) 25-28.

[42] J.C. Ye, L. Ajdelsztajn, J.M. Schoenung, Bulk nanocrystalline aluminum 5083 alloy fabricated by a novel technique: cryomilling and spark plasma sintering, Metall. Mater. Transac. A 37A (2006) 2569-2579.

[43] N. Allain-Bonasso, F. Wagner, S. Berbenni, D.P. Field, A study of the heterogeneity of plastic deformation in IF steel by EBSD, Mater. Sci. Eng. A 548 (2012) 56-63.

[44] V.M. Miller, T.M. Pollock, Texture modification in a magnesium-aluminum-calcium alloy during uniaxial compression, Metall. Mater. Trans. A 47 (2016) 1854-1864.

[45] C.D. Barrett, A. Imandoust, A.L. Oppedal, K. Inal, M.A. Tschopp, H. El Kadiri, Effect of grain boundaries on texture formation during dynamic recrystallization of magnesium alloys, Acta Mater. 128 (2017) 270-283.

[46] M.W. Liu, W. Gong, R.X. Zheng, J. Li, Z. Zhang, S. Gao, C.L. Ma, N. Tsuji, Achieving excellent mechanical properties in type 316 stainless steel by tailoring grain size in homogeneously recovered or recrystallized nanostructures, Acta Mater. 226 (2022) 117629.

[47] M. Moghaddam, A. Zarei-Hanzaki, M.H. Pishbin, A.H. Shafieizad, V.B. Oliveira, Characterization of the microstructure, texture and mechanical properties of 7075 aluminum alloy in early stage of severe plastic deformation, Mater. Charact. 119 (2016) 137-147.

[48] J.A. Li, H.J. Zhao, S.H. Deng, X. Liu, O.A. Ojo, L.N. Zhang, W.R. Li, Laser melting deposition of aluminium 7050 alloy: heat treatment, microstructure and mechanical properties, Mater. Sci. Tech. 38 (2022) 1266-1275.

[49] C.I. Chang, C.J. Lee, J.C. Huang, Relationship between grain size and Zener-Holloman parameter during friction stir processing in AZ31 Mg alloys, Scr. Mater. 51 (2004) 509-514.

[50] K. Kurabayashi, S. Tokita, Y.S. Sato, Effect of Ni addition on the interfacial strength of Al/Cu dissimilar welds produced by friction stir lap welding, Metals, 12 (2022) 453.

[51] T. Matsunaga, K. Takahashi, T. Kameyama, E. Sato, Relaxation mechanisms at grain

boundaries for ambient-temperature creep of h.c.p. metals, Mater. Sci. Eng. A 510-511 (2009) 356-358.

[52] J. Koike, R. Ohyama, T. Kobayashi, M. Suzuki, K. Maruyama, Grain-boundary sliding in AZ31 magnesium alloys at room temperature to 523 K, Mater. Transac. 44 (2003) 445-451.

[53] Z.R. Zeng, M.R. Zhou, P. Lynch, F. Mompiou, Q.F. Gu, M. Esmaily, Y.M. Yan, Y. Qiu, S.W. Xu, H. Fujii, C. Davies, J.F. Nie, N. Birbilis, Deformation modes during room temperature tension of fine-grained pure magnesium, Acta Mater. 206 (2021) 116648.